Mixed Matrix Carbon Stainless Steel (MMCSS) Hollow Fibres for Gas Separation

Diego R. Schmeda-Lopez,[1] Simon Smart,[1] Wilhelm A. Meulenberg,[2] João C. Diniz da Costa[1*]

[1]The University of Queensland, FIM[2]Lab – Functional Interfacial Materials and Membranes Laboratory, School of Chemical Engineering, Brisbane Qld 4072, Australia.

[2]Forschungszentrum Jülich, Institute of Energy and Climate Research (IEK-1), Wilhelm-Johnen-Strasse, 52425 Jülich, Germany.

Corresponding Author: J. C. Diniz da Costa; Tel: +61 7 3365 6960; Fax:+61 7 3365 4199; Email: j.dacosta@uq.edu.au

Abstract

This work reports the preparation and investigation of novel mixed matrix carbon stainless steel (MMCSS) membranes. The study involves the production of MMCSS hollow fibres using SS particles of 6, 10, 16 and 45μm in diameter, polyetherimide as a polymeric binder and pyrolysis using a N_2 inert atmosphere. As a result, the binder pyrolysed to carbon and was retained in the hollow fibre structure, filling the voids between the SS particles. Smaller SS particles (6μm) yielded a bi-modal pore size distribution and superior mechanical properties. An interesting morphological feature was the formation of honeycomb-like carbon structures between the SS particles, attributed to the densification of the hollow fibre during pyrolysis at 1050 °C. The MMCSS hollow fibres (6μm) delivered almost pure N_2 for the separation of a synthetic flue gas composition (13% CO_2 and 87% N_2). It was found that CO_2 had a strong affinity to the surface of the MMCSS materials (isosteric heat of adsorption of 38 kJ mol^{-1}) whilst N_2 was a non-absorbing gas. Therefore, CO_2 permeation was controlled by surface diffusion whilst N_2 was controlled by the faster Knudsen diffusion mechanism. For CO_2 feed concentrations in excess of 13%, the CO_2 diffusion increased as the excess CO_2 could not adsorb on the fully saturated surface of the MMCSS hollow fibres, thus slightly reducing the N_2 purity in the permeate stream.

Keywords: porous hollow fibres**,** mixed matrix membrane; carbon; stainless steel; gas separation.

1. Introduction

Inorganic membranes are a promising separation technology due to their thermal, chemical and mechanical stability. Conventionally, inorganic membranes are composed of a porous substrate, an interlayer and an active layer. These different components are produced in separated stages. The porous substrate is firstly produced, following by 2-4 interlayer deposition on the surface of the substrate to allow for a smooth deposition of the final active layers [1]. These manufacturing stages always require sintering or calcination at high temperatures which significantly increases production costs and the cost of the final membrane. So it is highly desirable to reduce the number of stages necessary to produce an inorganic membrane, and thereby make important savings on the overall membrane cost [2]. The production of ceramic hollow fibre membranes is generally straight forward as the 'green' or unsintered hollow fibres, a mixture of ceramic particles and polymeric binder, can be produce very cheaply and then undergo thermal sintering. Examples of hollow fibres in this category include dense ceramic perovskites [3-5], and porous hollow fibres made from silica [6], alumina [7], titania [8] or combinations of these [9].

Liu and co-workers [10] pioneered the development of metal porous hollow fibres based on nickel. Subsequently, stainless steel (SS) hollow fibres using micron sized SS powders have been reported [11-14]. The metallic hollow fibres were prepared by extruding a mixture of metal particles suspended in a polymer solution (generally PESf) through a spinneret which then coagulates in a phase inversion process, where water is commonly as the non-solvent phase. As with other inorganic hollow fibres the green fibres are sintered to create porous structures. These metallic hollow fibres are not brittle like prior ceramic versions and can withstand flexural stress up to ~600 MPa [11]. Recently, SS hollow fibres prepared with 6μm SS particles and polyetherimide (PEI) as the binder, further improved the mechanical strength to 1120 MPa [14].

Although SS hollow fibres are mechanically strong, their application in separation processes remains uncertain. The problem here is related to their morphological features - large pore sizes and broad pore size distribution. The nature of the solvent, polymer and non-solvent interactions in the phase inversion process [15-17], imbibe all hollow fibres, including SS hollow fibres, with finger-like and sponge-like pore structures. Pore sizes in the finger-like structures can be very large up to >200 μm, whilst the smaller pores in the sponge-like region were in the range of 3 - 5μm and sometimes submicron [14]. These pore structures are suitable as a support but not as a standalone membrane. Ideally, in order to lower production time and costs the final hollow fibre produced at the end of the sintering step would require little if any modification with additional layers.

To address this problem, this work proposes a mixed matrix carbon stainless steel (MMCSS) hollow fibre, where the binder is pyrolised in the hollow fibre matrix, thus filling the gaps between the SS particles and reducing pore sizes. The pyrolysis of carbon derived precursors has been used to prepare membranes for gas separation, including phenolic resins [18-21], composite alumina-phenolic resin [22-24], mixed matrix alumina phenolic resign [25], polyimides [26, 28] and binders used in hollow fibre preparation such as PEI and PESf [29-31]. Hence, this work reports the preparation and materials characterisation of MMCSS hollow fibres, in addition to gas adsorption and permeation.

2. Experimental

2.1. Materials, preparation and characterisation

Stainless steel AISI 316L of particle sizes 6, 10 and 16μm and AISI 410L of 45μm were purchased from Sandvik. Polyetherimide (PEI), produced by SABIC Innovative Plastics, was used as polymeric binder in the formation of the 'green' hollow fibres. Synthesis grade N-methyl-2-pyrrolidinone (NMP) from Sigma Aldrich was used as the solvent, whilst reverse osmosis filtered water (in house setup) was used as the non-solvent during the phase inversion step.

The production of the green fibre followed the method presented in a previous work [14]. Briefly, a polymer was used to bind the particles together to form the hollow fibre and retain the shape during sintering. This is most commonly accomplished through a phase inversion wet-dry spinning technique. For this method, the polymer was dissolved in the solvent over 2 days in a ratio of 1:3. Once the polymer was completely dissolved, the SS particles were added in the ratio 8.5:3:1 (SS : solvent : polymer) and the mixture stirred for several hours until the mixture was homogeneous and no lumps were observable. The mixture was degassed overnight, thus forming the spinning dope.

The spinning dope was then extruded through an orifice spinneret into a non-solvent bath (water), using a pressurised dry inert gas to push the slurry through. Upon reaching the bath, coagulation of the polymer / solids mixture occurred, consolidating the hollow fibre structure. The lumen of the hollow fibre was formed by concurrently injecting the non-solvent through the bore of the spinneret as the spinning dope was extruded into the non-solvent bath. An air gap, set to 45 mm, was found to be enough to produce the desired morphology. After spinning, the hollow fibres were left in the coagulation bath for 24 hours to finish the coagulation process. The sintering step was performed using a tubular furnace, MTI GSL-1600X, that allowed the flow of inert gases during the sintering step. The heating and cooling rates were kept at 5 °C min^{-1}. The sintering temperature was 1050 °C. Scanning Electron Microscopy (SEM) analysis was carried out on the surface morphological features

of the green and final pyrolised hollow fibres membranes. A JEOL JSM-7001F was used to obtain the SEM images, with a hot (Schottky) electron gun at accelerating voltage of 10 kV.

The MMCSS hollow fibres were characterized using a Shimadzu TGA-50 Thermogravimetric analyser (TGA) to determine mass loss as a function of the pyrolysis temperature. Mercury porosimetry was carried out using a Micromeritics AutoPore IV9520 to measure pores in the meso- and macropore size regions. Briefly, the mercury was intruded under pressure to the sample. This pressure values were directly converted into the corresponding pore size using the Washburn equation. For this analysis, the contact angle was set to be 130°, as recommended by Ellison et al. [32]. The key assumption of cylindrical pores was used and the maximum pressure reached was 415MPa (60,000psia). The lower pore size limit of measurement was 3nm.

The mechanical strength of the MMCSS hollow fibres was measured through a three-point bending test with an Instron 5543 universal testing machine. The strain rate was set at 1 mm min^{-1} and the sample span was 20 mm. The bending stress was calculated using the Eq. 1 as follows:

$$\sigma = \frac{8FKD_o}{\pi\left(D_o^4 - D_i^4\right)} \quad (1)$$

where σ is the bending stress (MPa), F is the load (N), K is the span (mm), D_o and D_i are the outer and inner diameters (mm), respectively.

2.2. Permeation tests

Single gas permeation was measured using a dead-end gas permeation rig. A hollow fibre membrane was placed in a module of small volume attached to a larger vessel of known volume pressurised with gas. The experiment began by opening the valve connecting the membrane module and the pressure vessel. The change in pressure in the permeate side was subsequently monitored over a period of time. The low pressure transducer (MKS Baratron 122BA-0100AB) measured the pressure in the permeate side, and the high pressure transducer (MKS Baratron 122BA-10000BB) measured the pressure in the feed side which was kept constant. The permeance can be calculated then using the following expression:

$$\left(P/l\right) = \frac{V}{ARTt} \quad (2)$$

where (P/l) is the permeance (mol s^{-1} $m^{-2}Pa^{-1}$), V is the volume (m^3), A is the membrane surface area (m^2), R is the universal gas constant (J K^{-1} mol^{-1}), T is the temperature (K) and t is time (s).

Binary gas permeation tests were carried out using a custom built rig. Briefly, gases were mixed using rotameters to control the volumetric flow, and the fraction of each gas was calculated using the universal law of gas. The feed, permeate and retentate compositions ware measured using a Shimadzu GC-2014 gas chromatograph (GC). A single MMCSS hollow fibre was placed in a module and in a furnace where the temperature was controlled by a PID temperature controller. The permeate and retentate mass flow were measured using a bubble flow meter, and the composition was measured using a GC. A mass balance was used to calculate the separation factor (α) [33], as described in the equations below.

$$m_{feed} = m_{permeate} + m_{retentate} \quad (3)$$

$$m_{feed}\, x_{feed,\,i} = m_{permeate}\, x_{permeate,\,i} + m_{retentate}\, x_{retentate,\,i} \quad (4)$$

$$\left(P/l\right)_i = \frac{m_{permeate}\, x_{permeate,\,i}}{\Delta P_i^{TM}} \quad (5)$$

$$\alpha_{i,j} = \frac{\left(P/l\right)_i}{\left(P/l\right)_j} \quad (6)$$

where m is the mass flow, x is the fraction of the component i in the stream, and ΔP_i^{TM} is the trans-membrane pressure difference.

3. Results and discussion

3.1. Materials Characterisation

The SEM images in Fig. 1 show that the geometrical shape of the MMCSS hollow fibre was generally maintained, though with minor shape variation. The morphology of the sintered fibre was mainly sponge-like at both inner and outer shells, whilst the middle formed large round macrovoid pores. These morphological features were similar to the green fibre, although the finger like pores at the inner shell of the green hollow fibre (Fig. 1a) disappeared during sintering/pyrolysis (Fig. 1b), consolidated into the larger macrovoids in the middle of the final MMCSS hollow fibre. The high magnification inset image (Fig. 1b) shows patterns like a honey comb structure where the SS particles are not clearly distinguishable. This SEM image suggests that carbon derived from the carbonisation or pyrolysis of the polymeric binder remained between the SS inter-particle regions, and at the same time covered the SS particles.

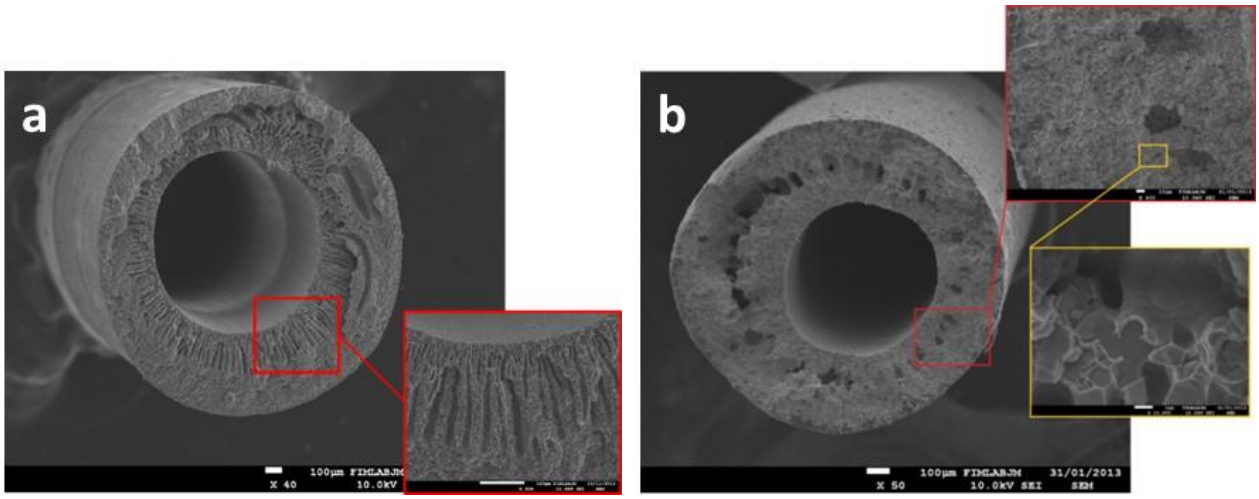

Fig. 1. Representative green (a) and carbon stainless steel (b) hollow fibre made with particles of 6μm.

The TGA analysis emulating the sintering/pyrolysis process in a nitrogen atmosphere of the MMCSS hollow fibres is displayed in Fig. 2. Initially the composition of the green fibre was 89.5 wt% SS particles and 10.5 wt% polymer. The TGA mass loss shows interesting results. The MMCSS hollow fibres prepared with the smaller SS particles (6, 10 and 16 μm, mean particle diameter) follow the same mass loss/gain trends, whilst the larger SS particle 45μm MMCMS hollow fibre had no mass gain between 750 and 900°C. Initially, the mass loss is consistent with the decomposition of PEI polymer binder which started at ~440°C and finished at ~640°C. The average mass losses up to 640°C were around 4% for all samples. From there, there was a major divergence as the samples prepared with the smaller SS particles gain weight to peak values up to 2.9 wt%, contrary to SS particle 45μm MMCSS hollow fibre which continued to lose weight. This difference is related to the austenitic steel 316L (SS particles 6, 10 and 16 μm) and the ferritic steel 410L (SS particle 45μm). Nitrogen is known to cause nitridation in austenitic stainless steels [34], thus forming chrome nitrides at high temperatures [35]. As the pyrolysis used nitrogen as the inert gas, these results suggest that the increase in mass at ~700 °C and peaking at ~900 °C may be associated with the reaction of nitrogen with the 316L SS particles. Nevertheless, from 900 °C to the final temperature of 1050 °C, the MMCSS hollow fibres prepared with the smaller SS particles followed a much faster mass loss rate than the 45μm MMCSS hollow fibre. These results suggest that the nitridation reversed, in agreement with the findings of Rawers et al. [36] where it showed that CrN was lost within this temperature range. This can be further noted that the final total mass losses for the smaller SS particle hollow fibers were ~5.0wt% and for the larger SS particle hollow fibre reached 5.8wt%, thus indicating that the final MMCSS hollow fibres contained in the region of 95.6wt% SS particles and at least 4.4wt% carbon, equivalent to 42% carbon retention.

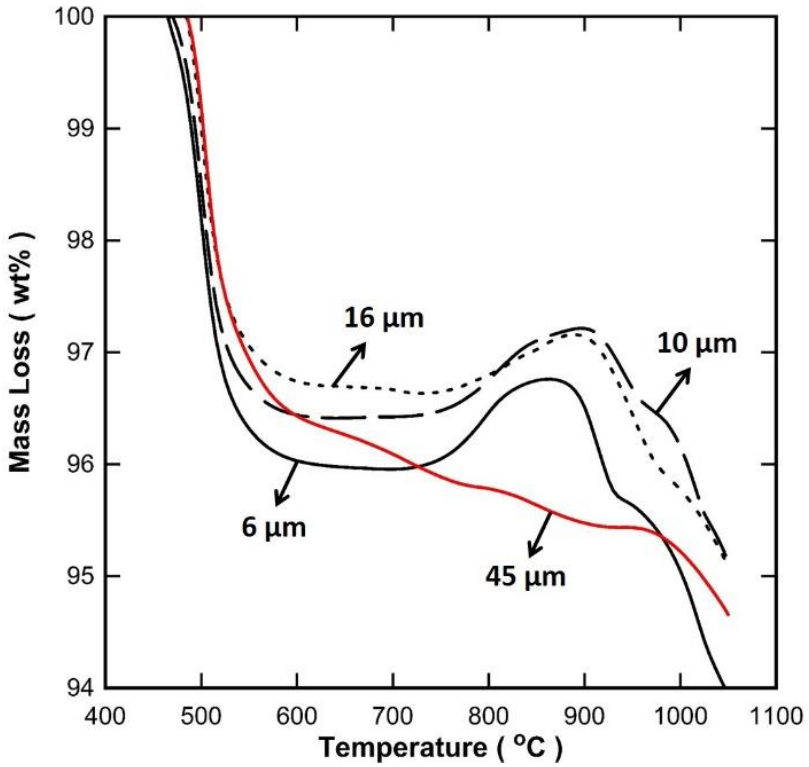

Fig. 2. Mass loss curves of MMCSS hollow fibres based on SS particle size.

Fig. 3 shows the pore radius as function of the cumulative porosity (pore volume / volume of the sample) and the pore size distribution derived from mercury porosimetry for all samples. There is a trend in terms of the pore size distribution. The 6µm MMCSS hollow fibres (Fig. 3a) resulted in a bimodal pore size distribution dominated by larger pore radius around 90µm related to macrovoids and a secondary porosity peaking at 0.04µm pore radius, related to smaller pores. As the particles sizes increased the bimodal distribution disappeared, with a tendency of smaller pore radius disappearing and new several peaks appearing at 0.1µm and shifting to higher pore radius for the 10µm SS particles (Fig. 3b), and even higher at 20µm for the 16µm SS particles (Fig. 3c). For the larger hollow fibre with the larger SS particles 45µm (Fig. 3d), the distribution at the smaller pores almost disappeared with a minor peak at ~1µm, though dominated by a peak of large macrovoids at 20 and 100µm. The total porosity increased by increasing the SS particle size within an experimental error of ±5% associated with the MMCSS doping mixture and pyrolysis process. For instance, total porosity increased from an average 15-20% for the smaller SS particle sizes (6 to 16 µm) to close to 30% for the larger particle size (45 µm). It is well known that volumes between particles increase as a function of their particle size. As the carbon content from the precursor binder was kept constant to SS, then the carbon content filled less of the interparticle-void as the particle size increase, thus also explaining the increase in total porosity.

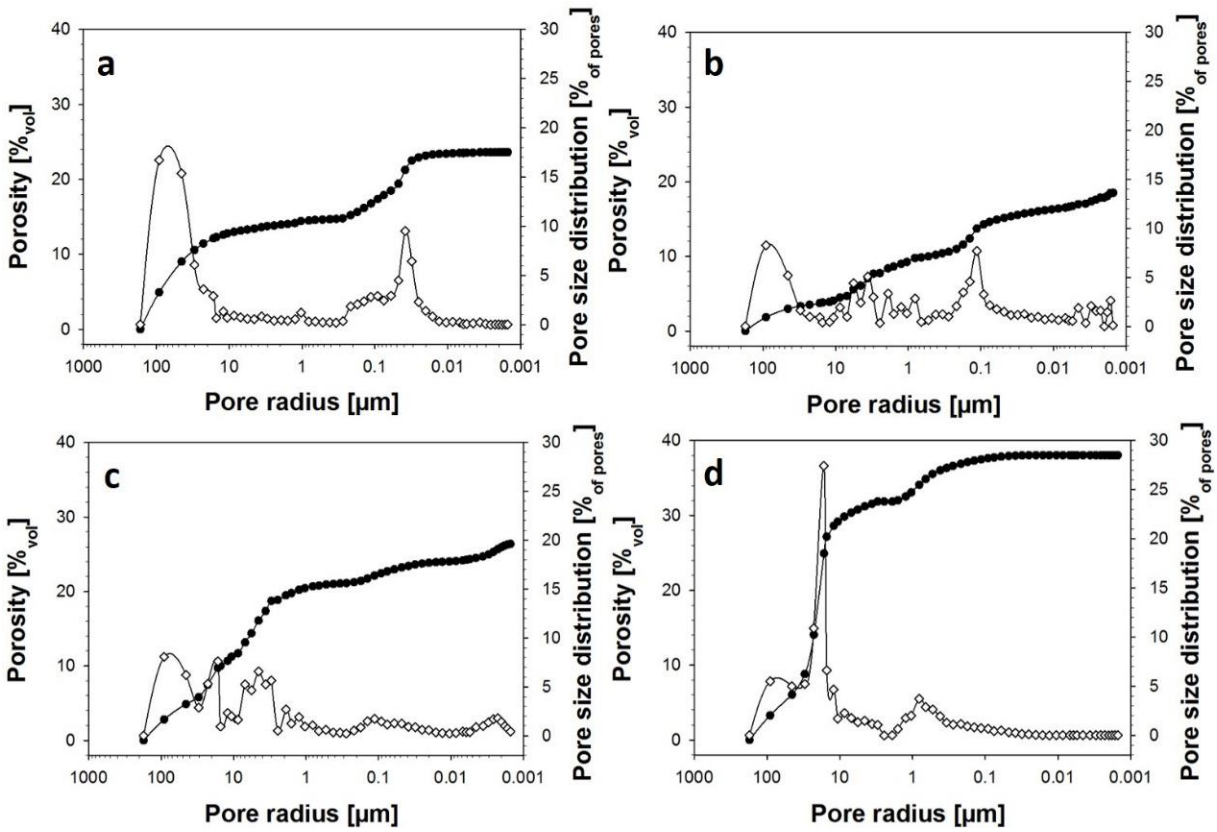

Fig. 3. Porosity (filled symbols) and pore size distribution (open symbols) of carbon stainless steel hollow fibres produced with particles of (a) 6µm, (b) 10µm, (c) 16µm and (d) 45µm.

The maximum flexural stress of the MMCSS hollow fibres in Fig. 4a shows a clear trend on the effect of particle size. For instance, samples made with 45µm particles could stand around 35MPa of strength, whilst the 6µm samples could stand almost four times this value, reaching stresses in the vicinity of 139 MPa. In similar fashion, the flexural strain in Fig. 4b shows that the ductility of the MMCSS hollow fibre prepared with 6µm SS particles was higher than the 45µm SS particle sizes, with average values of 0.005 and 0.0035 mm.mm-1, respectively. The mechanical trends are quite clear as increasing the SS particle size decreased both flexural stress and strain.

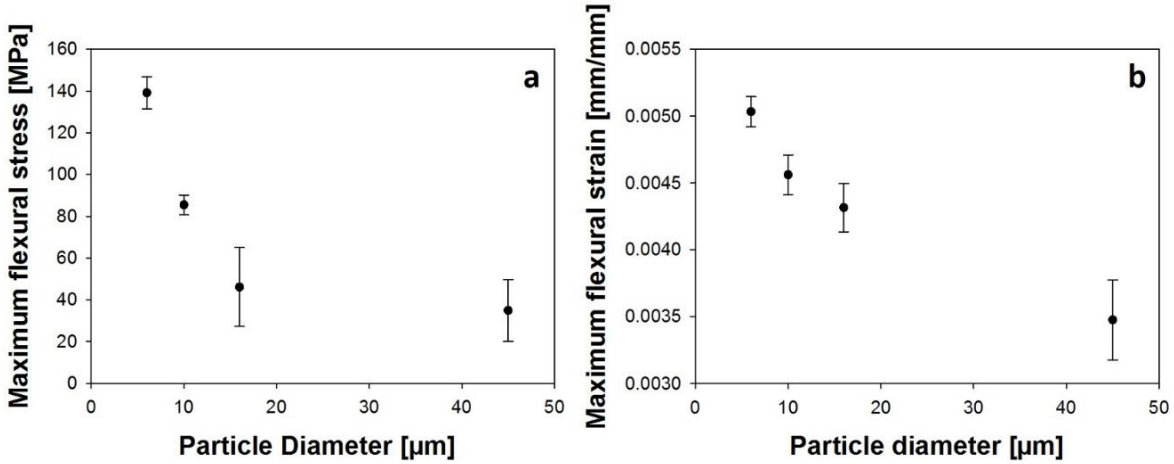

Fig. 4. (a) Maximum flexural stress and (b) maximum strain of MMCSS hollow fibres.

3.2. Gas transport properties

The MMCSS hollow fibres were initially tested for single gas permeation. The hollow fibres prepared with SS particles of 10, 16 and 45 µm did not yield any gas separation, and were no longer considered for gas permeation. Previous work on pure SS hollow fibres showed that the pore size increased as the SS particle size also increased [14]. As the polymeric binder to SS particle weight ratio was constant for all MMCSS hollow fibres, these results suggest that the pyrolysis of the polymer within the SS inter-particle space was not enough to confer carbon porous structures with properties for separating gases. Therefore, the performance of the MMCSS hollow fibres prepared with SS particles 6 µm were further investigated. Fig. 5 displays the gas permeance versus the temperature for He, N_2 and CO_2. These results clearly indicate that by increasing the temperature the gas permeance values decreased. Although the MMCSS hollow fibres were able to separate gases, the average He/N_2 permselectivity of 1.8 is lower than the Knudsen ideal permselectivity value of 2.65 for these gases. All these permeance results were measured at average of three points of short term testing of 1 hour.

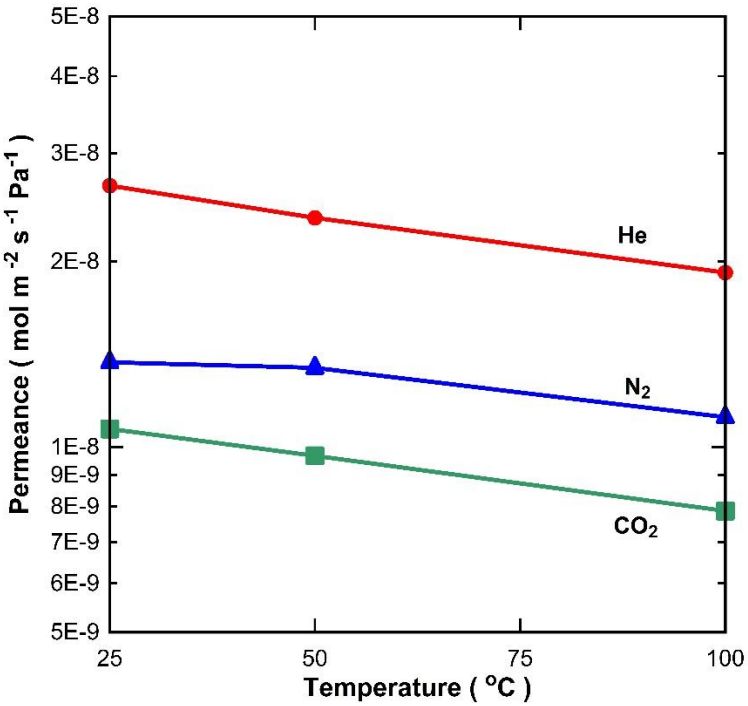

Fig. 5. Gas permeance at 0.25 MPa as function of temperature.

Longer term permeance testing was carried out to understand further the performance of the MMCSS hollow fibres. Fig 6a shows that the permeance of He and N_2 achieved steady state since the onset of experimental work. However, it is interesting to observe that the CO_2 permeance was not constant for the first 50 hours of permeation testing, with steady state being reached only after 50 hours. The average He/CO_2 and N_2/CO_2 permselectivities at steady state reached 17.5 and 5.0, respectively, well

above the ideal Knudsen selectivity values of 3.3 and 1.3. In principle, these permselectivity results could suggest that molecular sieving transport was occurring. However, as the gas permeance for all gases reduced with temperature (Fig. 5), this transport behaviour is not associated with activated transport, and more likely attributed to Knudsen diffusion. Furthermore, as the kinetic of diameter of CO_2 (d_k = 3.3 Å) is smaller than N_2 (d_k = 3.6 Å), then these results clearly indicate that pore size exclusion is not the transport mechanism. In this case, the Knudsen diffusion is combined with a strong surface sorption, where CO_2 has a stronger affinity to the surface of the MMCSS hollow fibre. To further test this point, the hollow fibres were characterised by volumetric gas adsorption. The CO_2 adsorption isotherms in Fig. 6b show reasonably strong CO_2 coverage in a linear relationship with pressure, which is consistent with Henry's law. The Arrhenius plot of the Henry's constant (lnK) versus T^{-1} yielded a relatively high CO_2 isosteric heat of adsorption (Q_{st}) equal to 34.8 kJ mol^{-1}. N_2 adsorption at 0 °C was almost negligible, and together with the non-adsorbing properties of He, demonstrates that the Q_{st} value for both N_2 and He is ~0 kJ mol^{-1}.

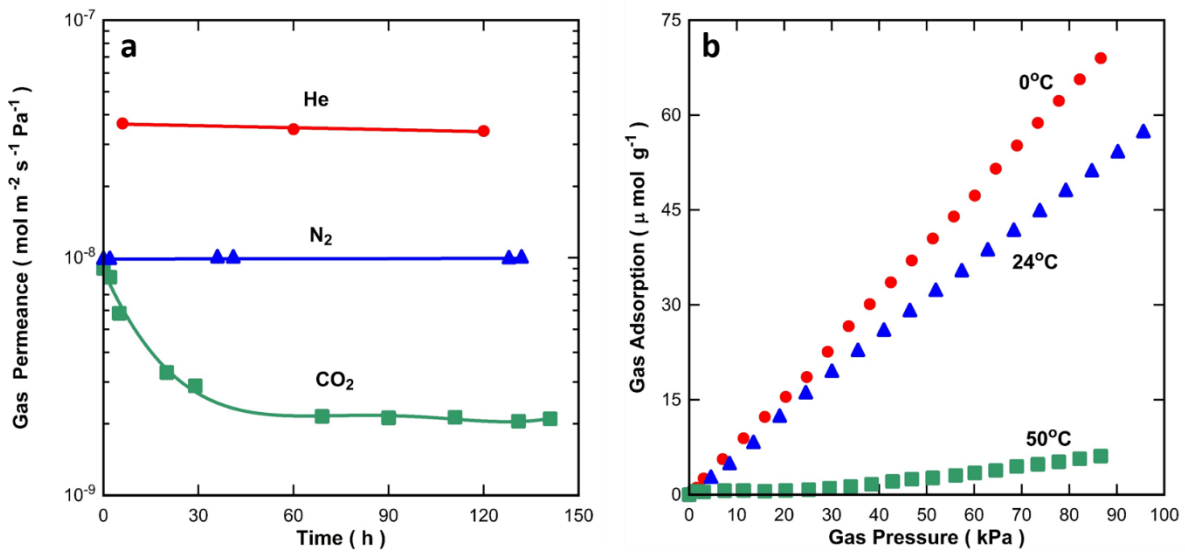

Fig. 6. (a) Single gas permeation at 0.4 MPa and 125 ºC of MMCSS membrane and (b) gas adsorption on MMCSS material.

As CO_2 and N_2 are common gases in the flue gas from coal power stations at temperatures above 100°C [37, 38], the MMCSS hollow fibres were tested for the separation of these gases as binary mixtures. It is noteworthy to observe in Fig. 7 that the MMCSS hollow fibre separated N_2 from a synthetic flue gas (13% CO_2 and 87% N_2) and consistently delivered very high N_2 purity in excess of 99% in the permeate stream from 75 to 125 °C. These results are further supported by the N_2 flux being ~70 times higher than the CO_2 flux. In principle, it would be expected a higher N_2 flux as the driving force (i.e. feed partial pressure) N_2 is 6.7 times higher than that of CO_2. However, as CO_2 has

a strong sorption affinity to the MMCSS hollow fibre, it is transport is dominated by surface diffusion which is generally slow as compared to Knudsen and molecular pore size diffusion where adsorption is weak. However, Fig. 8 shows that by increasing the CO_2 feed concentration, then the flux of CO_2 increased likewise, and the purity of N_2 decreased in the permeate stream. Therefore, these results strongly suggest that higher CO_2 feed concentrations (>13%) has CO_2 molecules in excess of those already adsorbed on the MMCSS hollow fibre matrix. Consequently, the excess CO_2 diffuses through the membrane similarly to N_2 diffusion.

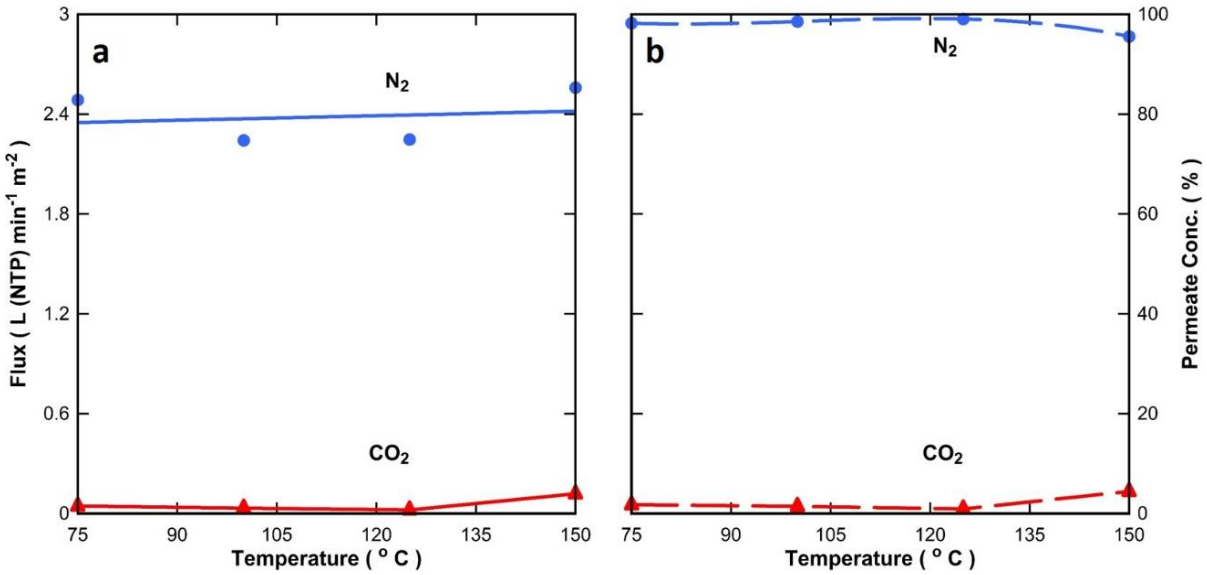

Fig. 7. (a) Gas flux (±8% of value) and (b) permeate concentration (±12% of value) as a function of temperature for a flue gas concentration of 13% CO_2 and 87% N_2 at 125 ºC. Gas flux (full line) and permeate concentration (broken line).

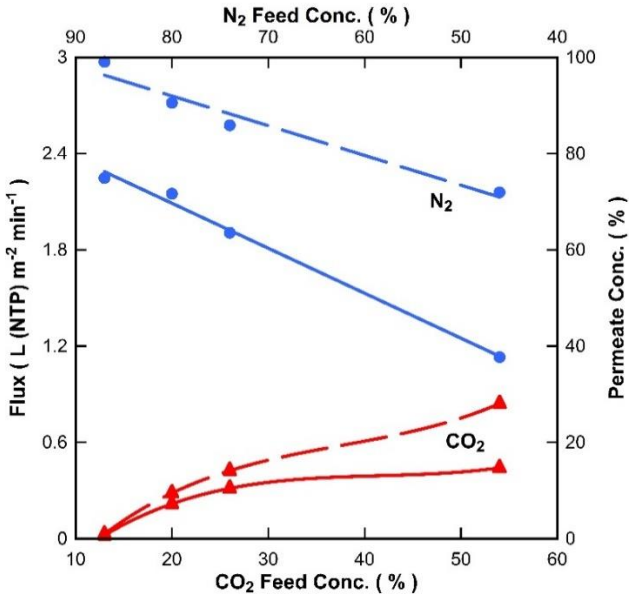

Fig. 8. Gas flux (±8% of value) and permeate concentration (±12% of value) as a function of CO_2 feed concentration at 125 ºC. Gas flux (full line) and permeate concentration (broken line).

3.3. Morphological features

It is interesting to observe in the SEM image (Fig. 1) the lack of finger-like structures, a common feature of hollow fibres derived from PESf or PEI using water as a coagulation bath. The finger-like structures were reported for perovskite [5], alumina [7], titania [8] and SS hollow fibres [11], particularly close to the inner shell, which is associated with the fast solvent/non-solvent de-mixing during coagulation [39-41]. However, the SEM image also shows that large round macrovoids prevailed in the centre of the hollow fibre wall. A schematic of the MMCSS hollow fibre pyrolysis/sintering is displayed in Fig. 9 to explain this process. Contrary to the conventional methods of preparation inorganic hollow fibres, where the polymeric binder is burnt out by pre-calcination in air, in this work the sintering was carried out in an inert atmosphere (nitrogen) where the polymeric binder was pyrolysed and the resultant carbon was essentially kept within the hollow fibre structure. The TGA results (Fig. 2) clearly shows that 4.4wt% carbon was kept after the pyrolysis/sintering process at 1050 °C, out of 10.5wt% polymeric binder in the green fibre. These results suggest that carbon remained within the structure of the MMCSS hollow fibres.

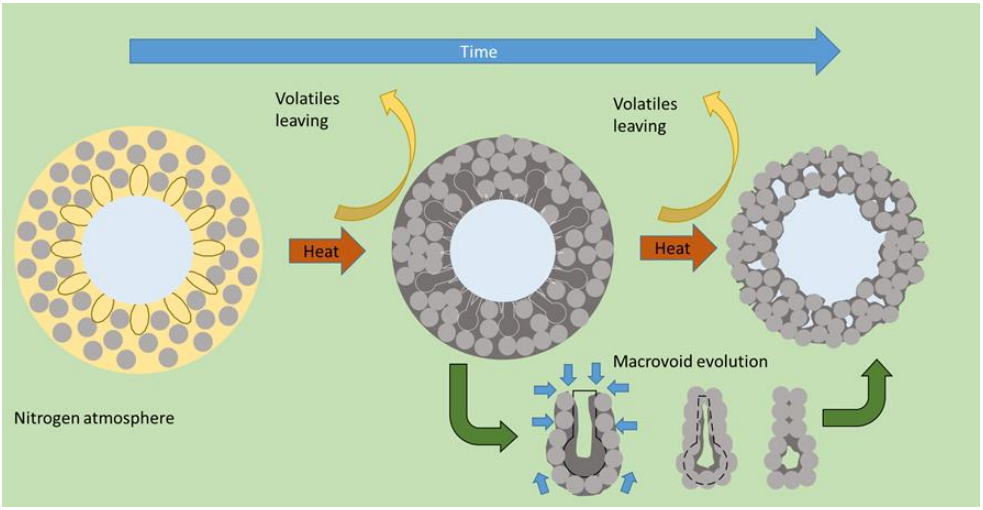

Fig. 9. Schematic of the MMCSS hollow fibre sintering / pyrolysis process.

During the pyrolysis/sintering up to 1050°C, the MMCSS hollow fibre external and internal diameter reduced by an average of 10 and 17% from the initial green fibre. This led to further densification of the hollow fibre, evidenced by wall thickness reduction of 10%. The carbon filled the SS inter-particle spaces. As the finger-like pores were predominantly closer to the inner shell, the densification in the inner shell brought the SS particles much closer than in the outer shell. In the case of the SS hollow fibres, the sintering process caused the particles to form necks and maintain the finger-like structures. However, in the case of the MMCSS membranes, carbon remains between the SS particles. Therefore,

the sintering and densification of the MMCSS membranes, coupled with carbon closer to the SS particles, led to the finger-like structures becoming less feasible closer to the inner shell. In the case of the large round macrovoids in the centre of the MMCSS hollow fibre, these pores are too large at the green fibre stage. Therefore, the lack of carbon filling coupled with not enough densification could no longer reduce the dimensions of these large pores. Hence, the MMCSS hollow fibres formed a combination of large round macrovoids and sponge like regions.

The MMCSS hollow fibres also show reasonable mechanical properties as compared to previous inorganic hollow fibres as listed in Table 2. For instance, minimum and maximum strength of 35 and 139 MPa are in the same range as those inorganic hollow fibres based on Al_2O_3, Ni and Ni/YSZ, though below those reported for pure SS hollow fibres ranging from 820 to 3500 MPa. The latter differences can be attributed to carbon which remained around the SS particles and therefore inhibited SS particle neck formation and reducing the overall mechanical strength of the hollow fibre. Other differences are associated with the sintering temperature, as higher temperatures tend to densify materials and increase mechanical strength.

Table 2. Comparison of mechanical strength of inorganic hollow fibres.

Material	**Sintering Temperature**	**Min Strength**	**Max Strength**	**Reference**
Al_2O_3	1300 – 1600 °C	21 MPa	304 MPa	[9]
Ni	1100 – 1300 °C	75 MPa	160 MPa	[17]
Ni / YSZ	1200 – 1400 °C	40 MPa	160 MPa	[34]
SS	1050 – 1200 °C	450 MPa	3500 MPa	[11]
SS	950 – 1100 °C	303 MPa	820 MPa	[14]
MMCSS hollow fibres	1050 °C	35 MPa	139 MPa	This work

A final structural feature of interest is the capability of the MMCSS hollow fibre to selectively separate N_2 and CO_2. The SEM images (Fig. 1) clearly show the formation of honeycomb structures. This unique future has never been previously observed in ceramic and metal hollow fibres, and neither in carbon hollow fibres prepared via the pyrolisation of polymeric hollow fibres. The honeycomb structure was obtained due to heat-sink property of the SS particles embedded into the polymeric binder. Under pyrolisation conditions, the SS particles were covered with the melted polymer. Concomitantly, the melted polymer formed honeycomb structures between the SS particles during pyrolisation until the melting polymer was fully carbonised at 1050°C. The obtained structures

resulted in He/N_2 permselectivity above Knudsen ideal selectivities, thus close and suggesting the gas transport was controlled by Knudsen diffusion. However, He/CO_2 and N_2/CO_2 permselectivity was higher reaching a value of 17.5 and 5.0, thus suggesting that the permeation of CO_2 was limited by a surface sorption and diffusion mechanism. This is schematically depicted in Fig. 10, as CO_2 surface coverage was high allowing CO_2 to adsorb on the surface of the MMCSS hollow fibre at the feed side, and diffuse along the internal surface structure of the hollow fibre all the way to the permeate side of the hollow fibre where CO_2 desorption occurred. As the isosteric heat of adsorption of CO_2 was strong at 38 kJ mol^{-1}, CO_2 required more energy to diffuse through the hollow fibre and leading to slower surface diffusion. In the case of N_2, its isosteric heat of adsorption was ~ 0 kJ mol^{-1}. Hence, N_2 could penetrate quite easily through the porous structure of the hollow fibre without sorption hindrance leading to much faster diffusion through the hollow fibre. Therefore, CO_2 permeation was controlled by the low surface diffusion mechanism whilst N_2 was controlled by the faster Knudsen diffusion mechanism for CO_2 feed concentrations below 13%. For higher feed concentrations (>13%), the surface was already fully saturated with adsorbed CO_2, and the excess CO_2 diffused through the membrane in a similar diffusion mechanism as N_2.

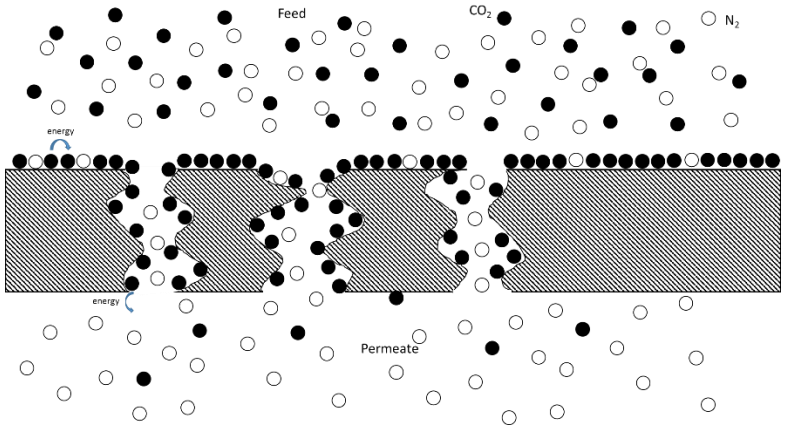

Fig. 10. Schematic showing the effect that adsorption has on selectivity.

4. Conclusions

A combined pyrolysis/sintering process allowed mixed matrix hollow fibres to be made from carbon and SS particles of 6, 10, 16 and 45µm in diameter. The mechanical properties of the hollow fibres increased as the SS particle size decreased, thus forming a denser structure confirmed by porosity tests. Approximately 42% of the original polymeric binder was retained as pyrolysed carbon within the pore structure of the MMCSS hollow fibre. In particular, the carbon frequently surrounded the SS particles forming honeycomb-like structures between the SS particles. In the case of the smallest SS particles (6 µm), which also had the correspondingly smallest pore size, these honeycomb-like carbon structures imparted some gas separation properties to the hollow fibre. The MMCSS hollow fibres

(6μm) delivered almost pure N_2 for the separation of a synthetic flue gas composition (13% CO_2 and 87% N_2) across a range of realistic flue gas temperatures. It was found that CO_2 had a strong affinity to the surface of the MMCSS materials (isosteric heat of adsorption of 38 kJ mol^{-1}) whilst N_2 was a non-absorbing gas. Therefore, CO_2 permeation was controlled by surface diffusion whilst N_2 was controlled by the faster Knudsen diffusion mechanism.

Acknowledgement

D.R. Schmeda-Lopez gratefully thanks the Chemical Engineering Scholarship at The University of Queensland. J. C. Diniz da Costa acknowledges the financial support given by the Australian Research Council (ARC) Future Fellowship Program (FT130100405).

References

[1] A.J. Burggraaf, L. Cot, Fundamentals of Inorganic Membrane Science and Technology, 1996, Elsevier Science Burlington.

[2] M. De Falco, L. Marrelli, G. Iaquaniello, Membrane reactors for hydrogen production processes, 2011, Springer New York.

[3] S. Liu, G.R. Gavalas, Oxygen selective ceramic hollow fiber membranes, J. Membr. Sci. 246 (2005) 103-108.

[4] S. Liu, G.R. Gavalas, G.R. Preparation of oxygen ion conducting ceramic hollow-fiber membranes, Ind. Eng. Chem. Res. 44 (2005) 7633-7637.

[5] P. Haworth, S. Smart, J. Glasscock, J.C. Diniz da Costa, High performance yttrium-doped BSCF hollow fibre membranes, Sep. Purif. Technol. 94 (2012) 16-22.

[6] J.D. Way, D.L. Roberts, Hollow fiber inorganic membranes for gas separations, Sep. Purif. Technol. 27 (1992) 29-41.

[7] S. Liu, K. Li, R. Hughes, Preparation of porous aluminium oxide (Al_2O_3) hollow fibre membranes by a combined phase-inversion and sintering method, Ceram. Int. 29 (2003) 875-881.

[8] X. Zhang, D.K. Wang, D.R. Schmeda-Lopez, J.C. Diniz da Costa, Fabrication of nanostructured TiO_2 hollow fiber photocatalytic membrane and application for wastewater treatment, Chem. Eng. J. 236 (2014) 314-322.

[9] S. Liu, G.R. Gavalas, Preparation TiO_2/Al_2O_3 composite hollow fibre membranes, J. Membr. Sci. 218 (2003) 269-277.

[10] B. Meng, X. Tan, X. Meng, S. Qiao, S. Li, Porous and dense Ni hollow fibre membranes, J. Alloys Comp. 470 (2009) 461-464.

[11] M.W.J. Luiten-Olieman, L. Winnubst, M. Wessling, A. Nijmeijer, N.E. Benes, Porous stainless steel hollow fiber membranes via dry–wet spinning, J. Membr. Sci. 370 (2011) 124-130.

[12] M.W.J. Luiten-Olieman, M.J.T. Raaijmakers, L. Winnubst, M. Wessling, A. Nijmeijer, N.E. Benes, Porous stainless steel hollow fibers with shrinkage-controlled small radial dimensions, Scripta Mater. 65 (2011) 25-28.

[13] B. Michielsen, H. Chen, M. Jacobs, V. Middelkoop, S. Mullens, I. Thijs, A. Buekenhoudt, F. Snijkers, Preparation of porous stainless steel hollow fibers by robotic fiber deposition, J. Membr. Sci. 437 (2013) 17-24.

[14] D.R. Schmeda-Lopez, S. Smart, E.H.M. Nunes, D. Vasconcelos, W.L. Vasconcelos, M. Bram, W.A. Meulenberg, J.C. Diniz da Costa, Stainless steel hollow fibres – Sintering, morphology and mechanical properties, Sep. Purif. Technol. 147 (2015) 379-387.

[15] L. Broens, F.W. Altena, C.A. Smolders, D.M. Koenhen, Asymmetric membrane structures as a result of phase separation phenomena, Desalination 32 (1980) 33-45.

[16] I-H. Choi, I.-C. Kim, B.-R. Min, K.-H. Lee, Preparation and characterization of ultrathin alumina hollow fiber microfiltration membrane, Desalination 193 (2006) 256-259.

[17] S.-M. Lee, I.-H. Choi, S-W Myung, J.-Y. Park, I.-C. Kim, W.-N. Kim, K.-H. Lee, Preparation and characterization of nickel hollow fiber membrane, Desalination 233 (2008) 32-39.

[18] G. Qin, C. Wang, W. Wei, Preparation of a mesoporous carbon membrane from resorcinol and formaldehyde, Carbon 48 (2010) 4206-4208.

[19] T.A. Centeno, A.B. Fuertes, Carbon molecular sieve membranes derived from a phenolic resin supported on porous ceramic tubes, Sep. Purif. Technol. 25 (2001) 379-384.

[20] W. Wei, G.T. Qin, H.Q. Hu, L.B. You, G.H. Chen, Preparation of supported carbon molecular sieve membrane from novolac phenol-formaldehyde resin, J. Membr. Sci. 303 (2007) 80-85.

[21] W.L. Zhou, M. Yoshino, H. Kita, K. Okamoto, Carbon molecular sieve membranes derived from phenolic resin with a pendant sulfonic acid group, Ind. Eng. Chem. Res. 40 (2001) 4801-4807.

[22] M. Teixeira, M.C. Campo, D.A. Pacheco Tanaka, M.A. Llosa Tanco, C. Magen, A. Mendes, Composite phenolic resin-based carbon molecular sieve membranes for gas separation, Carbon 49 (2011) 4348-4358.

[23] M.A. Llosa Tanco, D.A. Pacheco Tanaka, A. Mendes, Composite-alumina-carbon molecular sieve membranes prepared from novolac resin and boehmite. Part II: Effect of the carbonization temperature on the gas permeation properties, I. J. Hydrogen Energy 40 (2015) 3485-3496.

[24] M. Teixeira, S. Rodrigues, M. Campo, D.A. Pacheco Tanaka, M.A. Llosa Tanco, L. Madeira, J. Sousa, A. Mendes, Boehmite-phenolic resin carbon molecular sieve membranes-Permeation and adsorption studies, Chem. Eng. Res. Des. 92 (2014) 2668-2680.

[25] Y. Song, D.K. Wang, G. Birkett, W. Martens, S. Smart, J.C. Diniz da Costa, Mixed matrix carbon molecular sieve and Alumina (CMS-Al_2O_3) membranes, Scient. Rep. 6 (2016) 30703. DOI: 10.1038/srep3070

[26] Y. Kusuki, H. Shimazaki, N. Tanihara, S. Nakanishi, T. Yoshinaga, Gas permeation properties and characterization of asymmetric carbon membranes prepared by pyrolyzing asymmetric polyimide hollow fiber membrane, J. Membr. Sci. 134 (1997) 245-253.

[27] S.L. Fu, E.S. Sanders, S.S. Kulkarni, W.J. Koros, Carbon molecular sieve membrane structure-property relationships for four novel 6FDA based polyimide precursors, J. Membr. Sci. 487 (2015) 60-73.

[28] H. Wang, L. Zhang, G.R. Gavalas, Preparation of supported carbon membranes from furfuryl alcohol by vapor deposition polymerization, J. Membr. Sci. 177 (2000) 25-31.

[29] W.N.W. Salleh, A.F. Ismail, Carbon hollow fiber membranes derived from PEI/PVP for gas separation, Sep. Purif. Technol. 80 (2011) 541-548.

[30] W.N.W. Salleh, A.F. Ismail, Effect of stabilization temperature on gas permeation properties of carbon hollow fiber membrane, J. Appl. Polymer Sci. 127 (2013) 2840-2846.

[31] E. Barbosa-Coutinho, V.M.M. Salim, C. Piacsek Borges, Preparation of carbon hollow fiber membranes by pyrolysis of polyetherimide, Carbon 41 (2003) 1707-1714.

[32] A.H. Ellison, R.B. Klemm, A.M. Schwartz, L.S. Grubb, D.A. Petrash, Contact angles of mercury on various surfaces and the effect of temperature, J. Chem. Eng. Data 12 (1967) 607-609.

[33] A. Brunetti, G. Barbieri, E. Crioli, K.-H. Lee, B. Sea, D.W. Lee, WGS reaction in a membrane reactor using a porous stainless steel supported silica membrane, Chem. Eng. Proc. 46 (2007) 119-126.

[34] A.I. Nikonorova, F.R. Florensova, Nitriding of austenitic steels, Metal Sci. Heat Treat. 7 (1965) 636-638.

[35] R. Mariappan, S. Kumaran, T.S. Rao, Effect of sintering atmosphere on structure and properties of austeno-ferritic stainless steels, Mater. Sci. Eng. A 517 (2009) 328-333.

[36] J. Rawers, J.S. Dunning, G. Asai, R.P. Reed, Characterization of stainless steels melted under high nitrogen pressure, Metall. Mater. Trans. A 23 (1992) 2061-2068.

[37] M.K. Ram Reddy, Z.P. Xu, G.Q. Lu, J.C Diniz da Costa, Influence of water on high temperature CO_2 capture using layered double hydroxide derivatives, Ind. Eng. Chem. Res 47 (2008) 2630-2635.

[38] C.A. Scholes, K.H. Smith, S.E. Kentish, G.W. Stevens, CO_2 capture from pre-combustion processes—Strategies for membrane gas separation, I. J. Greenhouse Gas Control 4 (2010) 739-755.

[39] M. Mulder, Membrane preparation - Phase Inversion Membranes A2. In: Encyclopedia of Separation Science, Ed. I.D. Wilson, 2000, 3331-3346, Academic Press: Oxford.

[40] N. Yang, X. Tan, Z. Ma, A phase inversion/sintering process to fabricate nickel/yttria-stabilized zirconia hollow fibers as the anode support for micro-tubular solid oxide fuel cells, J. Power Sources 183 (2008) 14-19.

[41] X. Tan, S. Liu, K. Li, Preparation and characterization of inorganic hollow fiber membranes, J. Membr. Sci. 188 (2001) 87-95.